Chapter 7
Infrasound Signal Detection: Re-examining the Component Parts that Makeup Detection Algorithms

Omar Marcillo, Stephen Arrowsmith, Maurice Charbit and Joshua Carmichael

Abstract Detecting a Signal Of Interest (SOI) is the first step in many applications of infrasound monitoring. This intuitively simple task is defined as separating out signals from background noise on the basis of the characteristics of observed data; it is, however, deceptively complex. The problem of detecting signals requires multiple processes that are divisible at their highest level into several fundamental tasks. These tasks include (1) defining models for SOIs and noise that properly fit the observations, (2) finding SOIs amongst noise, and (3) estimating parameters of the SOI (e.g., Direction Of Arrival (DOA), Signal-to-Noise Ratio (SNR) and confidence intervals) that can be used for signal characterization. Each of these components involves multiple subcomponents. Here, we explore these three components by examining current infrasound detection algorithms and the assumptions that are made for their operation and exploring and discussing alternative approaches to advance the performance and efficiency of detection operations. This chapter does not address new statistical methods but does offer some insights into the detection problem that may motivate further research.

7.1 Introduction

The intuitively simple task of separating out signals from background noise on the basis of the characteristics of observed data or mathematical models is deceptively complex. Most infrasound applications exploits signal detection using array data and will be the focus of this chapter. The foundational theory on which array-based signal detectors have been built was constructed for radar and other applications

O. Marcillo (✉) · J. Carmichael
Los Alamos National Laboratory, Los Alamos, USA
e-mail: omarcillo@lanl.gov

S. Arrowsmith
Sandia National Laboratories, Albuquerque, USA

M. Charbit
Telecom Paris, Paris, France

A. Le Pichon et al. (eds.), *Infrasound Monitoring for Atmospheric Studies*,
https://doi.org/10.1007/978-3-319-75140-5_7

(see Krim and Viberg 1996 for a review). However, as most experts in the field are aware, the practice of applying the theory to infrasound data is often very challenging, particularly because the narrowband assumption fails. The wavelengths of infrasonic signals in the bandwidth required to monitor for large atmospheric explosion are large—between 3.5 and 0.35 km. At these distances, the conditions of the local atmosphere (temperature, wind speed, and direction) are variable, as are the characteristics of noise at each array element (Mack and Flinn 1971).

Most infrasound research in the area of signal detection has been driven by the inclusion of an infrasound network as part of the International Monitoring System (IMS) that is used to verify compliance with the Comprehensive Nuclear Test Ban Treaty (CTBT) Marty (2019). Arrays are an integral part of the design of the IMS infrasound network and early work provided constraints for array designs (Christie and Campus 2009; Marty 2019). Digital detector method developed for radar, seismology (Cansi 1995) and from image processing domains (Brown et al. 2008) were deployed to exploit the data from these arrays (Mialle et al. 2019). Most of these detectors operated under the assumption that the received signals associated a single SOI appear, the sensor level, as filtered versions of a same signal. This assumption is called perfect coherence. A particular case of interest for infrasound source is the case where the received signals are delayed/attenuated versions of a same signal. The other most commonly used assumption is that the noise is Gaussian, temporally and spatially white. All these assumptions lead to simple algorithms whose trade-off between false alarms and missed detections can be clearly quantified.

However, there are many other coherent sources of infrasound routinely detected by the IMS, such as microbaroms (Stopa et al. 2011; Landès et al. 2012; Walker 2012; Ceranna et al. 2019) and some volcanic activity (Dabrowa et al. 2011; Matoza et al. 2019). Such infrasound sources are often of no interest to verifying compliance with the CTBT. Rather, they are often considered nuisance sources. Compounding this problem, the perfect coherence of infrasound signals is often lost by propagation (Mack and Flinn 1971; Nouvellet et al. 2013; Green 2015). As detectors are included in pipeline processing, more sophisticated algorithms are needed to identify the signals of interest amongst permanent sources of coherent noise (e.g., microbaroms). Practical approaches that have been proposed included detection categorization algorithms (Brachet et al. 2010; Mialle et al. 2019) and adaptive thresholds (Arrowsmith et al. 2009). However, while these approaches have enabled the construction of event catalogs (Arrowsmith et al. 2015), they leave significant limitations. In particular, there remains a disconnect between the simplistic assumptions exploited by detection theory and practice for infrasound data processing. This chapter does not address new statistical methods but does offer some insights into the detection problem that may motivate further research.

This chapter is organized to show the different components involved in infrasound signal processing for detection purposes. We will examine these components in the following subsections of this chapter: (1) defining signal and noise models, (2) detecting signals in noise, and (3) parameter estimation/extraction.

7.2 Examining the Component Parts of Detectors

The term "detection" implies the process of finding something that is hidden. For our specific purposes, we extend the action of finding within detection to extracting features (parameters) that are used to characterize signals. Infrasound monitoring processes a stream of infrasound array data and performs detection by (1) defining noise and signal characteristics, (2) identifying signals of interest (SOI) that are distinct from noise, and (3) extracting parameters that characterize the SOI (Fig. 7.1). In most cases, the noise and SOI are quantitatively similar, therefore, signal separation, and parameter extraction prove challenging.

7.3 Defining Signal and Noise

Noise can be defined as attending to one or a combination of various criteria, such as coherence, power, origin, frequency content, or duration. We define two types of noise, namely, (1) physical and (2) operational noise. For array data, physical noise is any signal that is incoherent across the elements of the arrays. This definition includes very local pressure fluctuations generated by wind (Morgan and Raspet 1992) and intrinsic sensor self-noise. Infrasonic arrays typically have sensors separated at distances much larger than the mean size of turbulence, and thus turbulence is incoherent. These disturbances can propagate across elements (for the ones separated short distances) at lower speeds (Fehr 1967) than the speed of sound that we can distinguish and filter them out. Infrasonic signals that are coherent across the array might be considered noise depending on monitoring objectives, and we refer to these coherent signals as operational-type noise. Microbaroms (Donn and Naini 1973), for example, are a type of signal that are coherent but are considered noise for most

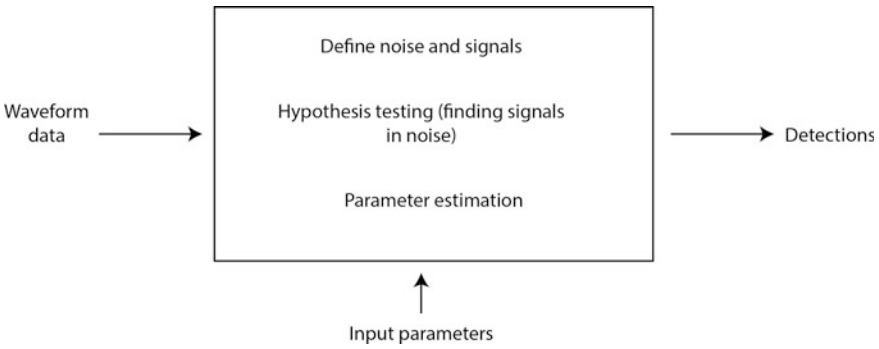

Fig. 7.1 The high-level components of infrasound signal detection algorithms. Differentiating signals from noise requires us to define parameters (dimensions) that can distinguish between the two

studies (Bowman et al. 2005). Figure 7.2 shows 24 h of data from one array element of a station of the IMS network (IS57, US) along with wind measurements from a collocated weather station to illustrate the variability of the infrasonic background noise and its relation to changing atmospheric conditions. The first 15 h of the day are characterized by a low-amplitude signal with amplitude below a tenth of a Pascal and wind speeds averaging between 2–3 m/s and a wide range of directions between −20° and 70°. The Power Spectral Density (PSD) of the overpressure waveform of a representative section of this period (cyan region) shows the very distinctive microbarom peak center at 0.2 Hz (Bowman et al. 2005) and multiple sharp peaks

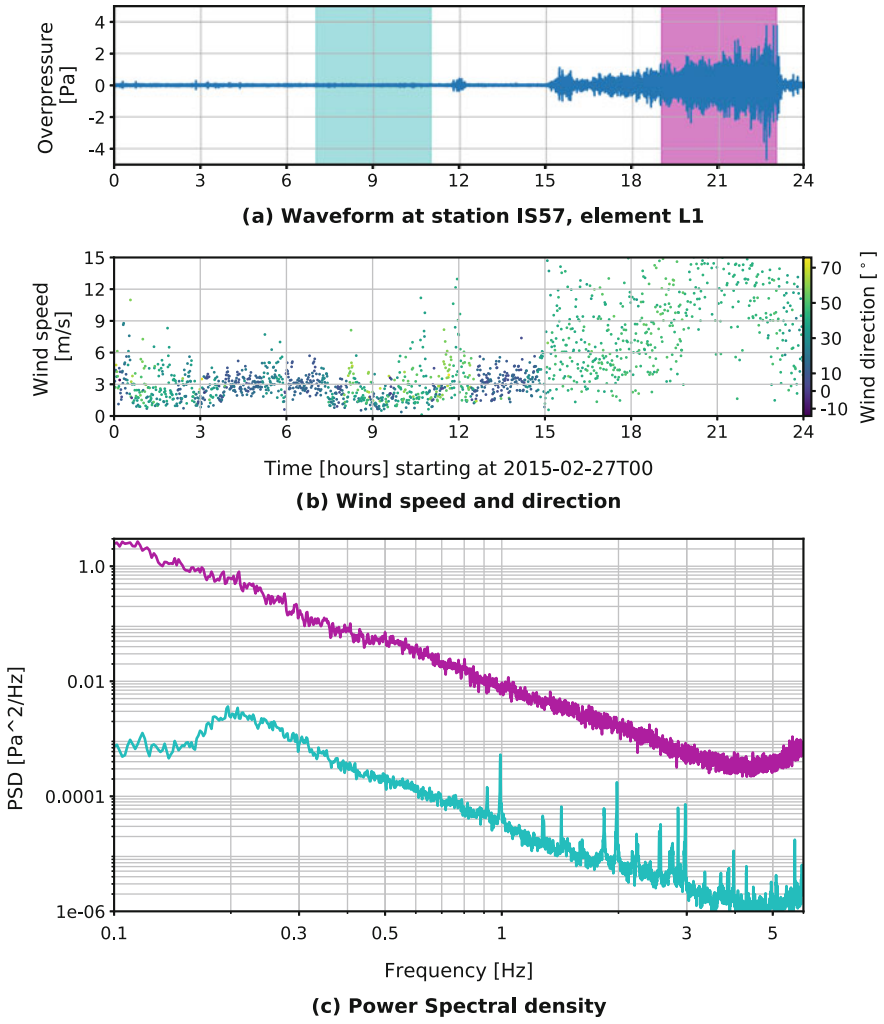

Fig. 7.2 Waveform and weather conditions for station IS57, element I57L1

above 0.9 Hz. Most of these peaks repeat at integer multiples of the first four peaks and may be related to sound from wind turbines (Marcillo et al. 2015; Pilger and Ceranna 2017). After hour 15 the amplitude of the overpressure increases with increasing wind speeds. Note also that wind direction after hour 15 is more stable between 40° and 50°. The PSD for a representative section of this period (magenta region) shows the typical characteristics of wind-induced noise that completely masks the other elements of the background noise.

Figure 7.3 shows array processing results (back-azimuth estimation) of the 24-h period described above. Two regions, before and after hour 15, are clearly separated in the coherence and the back-azimuth estimation maps. The microbarom and wind-turbine regions (around 0.2 Hz and above 0.9 Hz, respectively) show the highest values for coherence and stable back-azimuth estimations. The region after hour 15, where the signal is dominated by wind-induced noise, displays (as expected) very low coherence and a wide distribution for the estimation of back azimuths. This example shows two intervals with background noise with very different characteristics that resemble our definitions of operational- and physical-type noises.

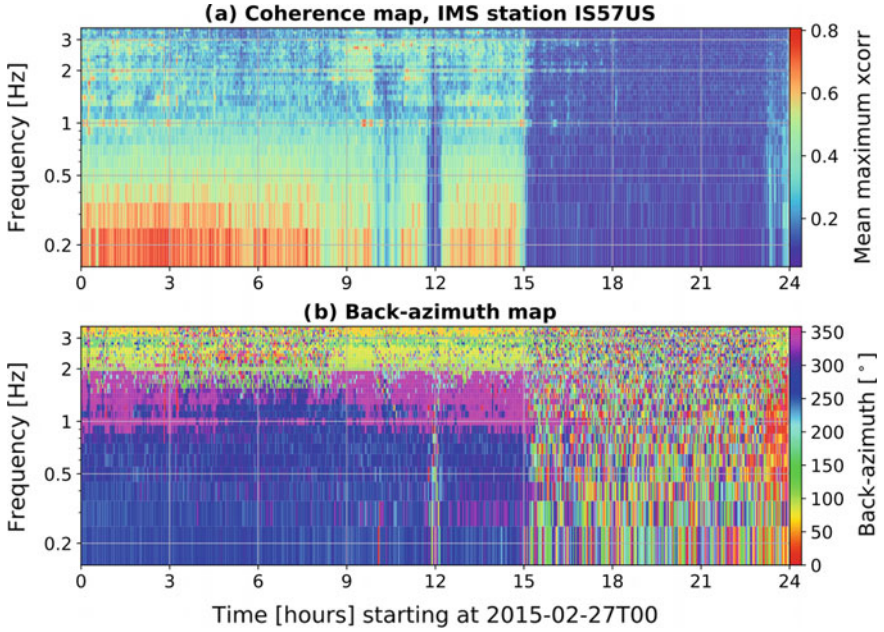

Fig. 7.3 Physical and Operational noise. 24 h of data from IMS station IS57 (Pinon Flats, California, US) that were processed using the Bartlett beamformer. The frequency bands were between 0.1 and 4 Hz with 0.1 Hz steps, a 200-s window, and 50% overlap. Panel **a** shows a map of the average maximum cross-correlation. Back azimuths are determined for each subwindow in each frequency using the maximum F-value criteria (Panel **b**)

In order to detect nuclear explosions (e.g., IMS network) exceeding a certain yield, definitions of signal have to be clarified. Given the sparsity of the 60-array network within the IMS network, SOIs triggered by nuclear explosions have generally propagated great distances (typically 100's–1000's to 10,000's of kilometers) through atmospheric waveguides (typically the stratospheric waveguide) (Drob et al. 2003). Infrasound SOIs, per our current definition, originate from atmospheric nuclear tests (Don and Ewing 1962; Donn and Ewing 1962; Dahlman et al. 1971), large chemical explosions (Ceranna et al. 2009; Green et al. 2011; Fee et al. 2013), large vulcanian eruptions (Fee and Matoza 2013; Matoza et al. 2019), and bolides that explode as terminal bursts (Le Pichon et al. 2013; Silber and Brown 2019). Acoustically, these signals are indistinguishable from nuclear detonations. Our definition of SOI excludes real infrasound waves from a wide-variety of natural and man-made sources including local events that are not detected at 100's to 1000's of kilometers (e.g., small charge explosions (Arrowsmith and Taylor 2013; Taylor et al. 2013), thunder (Anderson et al. 2014), moving vehicles) and continuous wave sources (e.g., wind farm (Marcillo et al. 2015; Pilger and Ceranna 2017) and anthropogenic noise). All of these excluded signals are now part of a refined concept of operational-type noise, which includes interference for unwanted coherent signals and random pressure fluctuations. To detect nuclear events, we must screen out the cacophony of infrasound from local and continuous wave sources, which are not applicable to the International Data Center (IDC) monitoring mission, and can be falsely associated at the network level to form spurious events (Arrowsmith et al. 2015). While they may be of general scientific interest, to consider such infrasound as signals results in too many false alarms when processing data on the sparse IMS network.

To formalize the discussed ideas about signals and noise we formulate the concept as a mathematical model. This modeling starts with array observations (multichannel data) that consist of M waveforms associated to the M elements of an array that are described by $x(t) = [x_1(t), x_2(t), \ldots, x_M(t)]^T$, where $x_m(t)$ $(1 \leq m \leq M)$ denotes an infrasound record measured on sensor m. In the presence of a SOI located far from the sensor array, a planar wave propagates across the array with a slowness vector $\boldsymbol{\theta} = (\theta_x, \theta_y, \theta_z)$ and an associated signal $s(t)$. Signal $s(t - \tau_m(\boldsymbol{\theta}))$ defines the waveform observation at the mth element of this array with a propagation delay τ_m:

$$\tau_m(\boldsymbol{\theta}) = r_m^T \boldsymbol{\theta}, \tag{7.1}$$

where $\boldsymbol{r}_m$ is the 3D location of the mth element.

In the presence of additive noise $w_m(t)$, we have:

$$x_m(t) = s(t - \tau_m(\boldsymbol{\theta})) + w_m(t) \tag{7.2}$$

The noise vector $w(t) = [w_1(t), w_2(t), \ldots, w_M(t)]$ is assumed to be a stationary spatially and temporally white random process, i.e., for any m, m', t, and t':

$$E\left(w_m(t), w_{m'}\left(t'\right)\right) = \sigma^2 \delta\left(t - t'\right)\delta_{mm'}, \tag{7.3}$$

where $\boldsymbol{E}$ is the expected-value operator, σ the standard deviation, δ_m the Kronecker's symbol, and $\delta(t)$ the Dirac's function. $w(t)$ is the realization of our definition of physical-type noise. This signal model with a coherent signal of interest and an incoherent noise can be expanded for a more realistic case if an interfering coherent (it can also be continuous) signal $v(t)$ (which is not of interest) is superimposed with the noisy SOI. The signal at the m-th element can be written as follows:

$$x_m(t) = s(t - \tau_m(\boldsymbol{\theta})) + v(t - \xi_m) + w_m(t), \tag{7.4}$$

where the term $v(t - \xi_m) + w_m(t)$ is now a realization of an operational-type noise. As our observations are based on discrete measurements of the wavefield, the sampling theorem can be applied to these continuous-time models to construct discrete-time versions. To apply this theorem, we assume that the continuous signals are band limited with the maximum frequency components f_m and that the recording system sampling rate (f_s) of the signals is $f_s \geq 2f_m$. With these assumptions, discrete version of Eq. 7.2 can be written as follows:

$$x_{n,m} = s_{n,m}(\boldsymbol{\theta}) + w_{n,m} \tag{7.5}$$

where $s_{n,m}(\boldsymbol{\theta}) = s(nT_s - \tau_m(\boldsymbol{\theta}))$, the integer $n = 0, \ldots, N-1$, and $T_s = 1/f_s$. In the rest of this manuscript, we will use the notation $x_n = [x_{n,1}, x_{n,2}, \ldots, x_{n,M}]^T$, $\boldsymbol{s}$ the sequence $s(0)$, $s(T_s)$, …, $s((N-1)T_s)$, and $s_n(\boldsymbol{\theta}) = [s_{n,1}(\boldsymbol{\theta}), s_{n,2}(\boldsymbol{\theta}), \ldots, s_{n,M}(\boldsymbol{\theta})]^T$. It is worth to notice that $s_n(\boldsymbol{\theta})$ depends only on $\boldsymbol{s}$ and $\boldsymbol{\theta}$ and can be denoted $s_n(s, \boldsymbol{\theta})$.

7.4 Detecting Signals Embedded in Noise

The main task in this step of processing infrasound records involves a binary test between the presence or absence of a noisy SOI in the data. Statistical inference analysis can be used to test the hypothesis of the absence of a SOI. The M-length vectors x_n are assumed to be independent and identically distributed (i.i.d.) with probability density function $f(x_n|\mu)$, where the parameter vector μ includes $\boldsymbol{\theta}$, σ^2, and $\boldsymbol{s}$ and belongs to the full parameter set $\chi = (R \times R \times R), R^+, R^N$. The "noise only" hypothesis H_0 is the subset χ_0 of χ such that $s = 0$. The counter-hypothesis is $H_1 = \chi - H_0$ and refers to the noise plus SOI hypothesis in the subset χ_1. To test H_0, a common approach consists of comparing a real-valued function (test statistic) based on the full observation $X = (x_1, x_2, \ldots, x_N)$ to a given threshold. The two competing hypotheses are expressible in general form as follows:

$$\begin{cases} H_0: X \sim f(x|\mu), \mu \in \chi_0 \\ H_1: X \sim f(x|\mu), \mu \in \chi_1 \end{cases} \tag{7.6}$$

Binary hypothesis testing will make the correct decision or incur an error by rejecting H_0 when it is true (type I error) or accepting H_0 when it is false (type II error). The next sections present a few test statistics that are commonly used in infrasound detection research. Section 7.6, in particular, quantifies performance comparisons between test statistics using Receiver Operating Characteristics (ROC) curves.

7.4.1 Tests Based on Construction of a Likelihood Function

A common test statistic for hypothesis testing based on the construction of likelihood functions is the Generalized Likelihood Ratio Test (GRLT). We construct these signal detectors from log-likelihood functions, whereby we replace the unknown source and noise parameters $\mu \in \chi_i$ in each PDF with their maximum likelihood estimates $\hat{\mu}_i = \arg\max_{\mu \in \chi_i} f(x|\mu)$. The ratio of logarithmic ratio of the resultant PDFs defines a scalar screening statistic $S_{GLRT}(x)$ (Kay 2013; Charbit 2017):

$$S_{GLRT}(x) = \frac{\max\limits_{\mu \in \chi} \sum_{n=1}^{N} \log(f(x_n|\mu))}{\max\limits_{\mu \in \chi_0} \sum_{n=1}^{N} \log(f(x_n|\mu))}, \tag{7.7}$$

where the log function is the natural (base e) logarithm. We explicitly decide if an SOI is present by comparing the size of $S_{GLRT}(x)$ to a threshold for event declaration γ. This comparison forms the log generalized likelihood ratio test, or log GLRT

$$S_{GLRT}(\boldsymbol{X}) \underset{H_0}{\overset{H_1}{\gtrless}} \gamma \tag{7.8}$$

To objectively select γ, we apply the Neyman–Pearson criteria, which estimates a value for γ that is consistent with a prescribed false alarm probability, $Pr_{FA} = \alpha$. This probability Pr_{FA} measures the rate at which Eq. 7.8 would choose H_1 when H_0 is true

$$\max_{\mu \in \chi_0} Pr_{FA}[S_{GLRT}(X) > \gamma|\mu] = \alpha \tag{7.9}$$

The scalar α measures the probability of identifying a non-existing signal event and is conventionally called the false alarm on noise, or just the false alarm probability. The explicit form of $S_{GLRT}(X)$ that includes maximum likelihood estimates of the competing PDFs was derived by Blandford (1974) and is expressed as follows:

$$F(X,\boldsymbol{\theta}) = \frac{\frac{1}{M}\sum_{n=1}^{N}\left(\sum_{m=1}^{M} x_{n,m}(\boldsymbol{\theta})\right)^2}{\frac{1}{M-1}\sum_{n=1}^{N}\sum_{m=1}^{M}\left(x_{n,m}(\boldsymbol{\theta}) - \frac{1}{M}\sum_{m=1}^{M} x_{n,m}(\boldsymbol{\theta})\right)^2} \tag{7.10}$$

To form this ratio, we first beamform waveform data using time delays that are defined in $\boldsymbol{\theta}$ space, then maximize the coherence of the resultant sum. We then compute the energy of this resultant waveform stack, as well as the residual beam energy. When waveform sample data are Gaussian distributed, this ratio has a noncentral F-distribution at every sample and is, therefore $F(X,\boldsymbol{\theta})$ is called the F-detector statistic. This detection statistic and the decision rule (Eq. 7.8) often give higher than predicted false alarm rates (when applied to real data) because the assumption of the Gaussian distribution of the noise is not realistic. Microbaroms can spectrally overlap with SOIs leading to inflation of the F-detector statistic and an increased type I errors (false alarms).

7.4.2 Tests Based on the Time Difference of Arrival (TDOA)

We can derive test statistics from the times of arrival of a SOI to the array elements. Tests using TDOA are based on estimating the time difference of arrival $\Delta t_{k,l}$ of a signal to a sensor pair (k, l). $\Delta t_{k,l}$ can be estimated using cross-correlation as follows:

$$\widehat{\Delta t}_{k,m} = \underset{\varrho}{\operatorname{argmax}}\left(\sum_{i} x_{i,k}x_{i+\varrho,m}\right)T_s \tag{7.11}$$

Examples of tests using TDOA are the Progressive Multichannel Correlation (PMCC) detector (Cansi 1995) and the Maximum Cross-Correlation Method (MCCM) (Lee et al. 2013).

The PMCC algorithm (Cansi and Pichon 2008) is a detector widely used in infrasound research (Brachet et al. 2010) which tests the consistency of arrival times of signals across the array. The relationship $r_{kmp} = \Delta t_{k,m} + \Delta t_{m,p} + \Delta t_{p,k}$ defined for a sensor triad (k,m,p) is the main component of the PMCC algorithm. $r_{kmp} = 0$ if a signal is present (closure relationship) and $r_{kmp} \neq 0$ in the presence of physical-type noise. r_{kmp} is estimated for all possible triads in the array. The consistency (C_κ) for a subnetwork with κ elements ($\kappa \leq M$) is defined as follows:

$$C_\kappa = \sqrt{\frac{6}{(\kappa-1)(\kappa-2)} \sum_{1 \le k < m < p < \kappa} \hat{r}_{kmp}^2} \tag{7.12}$$

PMCC defines a threshold to trigger detection for this subnetwork. If a detection is triggered, additional elements of the array are progressively added to the initial subnetwork and a test is run to assert that the new element can be added to the detection. This detection schema generates independent elementary detections (or PMCC pixels) at different frequency bands and time windows (Brachet et al. 2010; Mialle et al. 2019). These pixels are linked based on similarity into a frequency–time detection or PMCC family. Note that the distribution of C_κ is not known and also that its magnitude does not depend on the noise levels. The MCCM (Lee et al. 2013) tests the average of the maximum value of the normalized cross-correlation (Neidell et al. 1969) between all sensor pairs against a threshold.

7.4.3 Enhancements to the Classical Approach

Several enhancements to the classical approach described above can be identified. First, the signal and noise models along with the detectors, are formulated only in terms of some measure of the coherence of waves across an array. Second, while the detectors account for physical-type noise, they do not properly account for operational-type noise because they assume gaussianity and stationarity. To mitigate these limitations, different strategies have been adopted to operationalize coherence-based signal detectors in order to account for operational-type noise. One strategy is to implement a post-detection categorization algorithm to screen signals of interest from operational-type noise on the basis of additional properties of the waveforms (e.g., frequency) or the detection itself (e.g., detection duration) (e.g., Brachet et al. 2010). Another approach is the use of adaptive strategies to adjust detector thresholds on the basis of the characterization of elements of the operational-type noise (e.g., Arrowsmith et al. 2009). For example, in the presence of correlated noise, such as microbaroms, the F-statistic is distributed as $cF_{2BT,2BT(M-1)}$, where B is the bandwidth, T is the time window, M the number of sensors, $c = 1 - MP_c/P_u$, and P_c/P_u is the ratio of correlated to uncorrelated noise power (Shumway et al. 1999). Arrowsmith et al. (2009) implemented an algorithm to scale the distribution $cF_{2BT,2BT(M-1)}$ with a $1/c$ value so the new distributions follow traditional $F_{2BT,2BT(M-1)}$. This procedure allows the estimation of a detector threshold to find detections with a specified statistical significance in the presence of coherent noise. Updating the c value regularly allows the detector to adapt to temporal changes in noise. Figure 7.4 shows an example of detections based on the dynamic F-Statistics (magenta area) for the case of infrasound signals from a bolide. The F-values average a number between 3.5 and 4. These high F-values are most likely related to microbaroms and would trigger events continuously with high

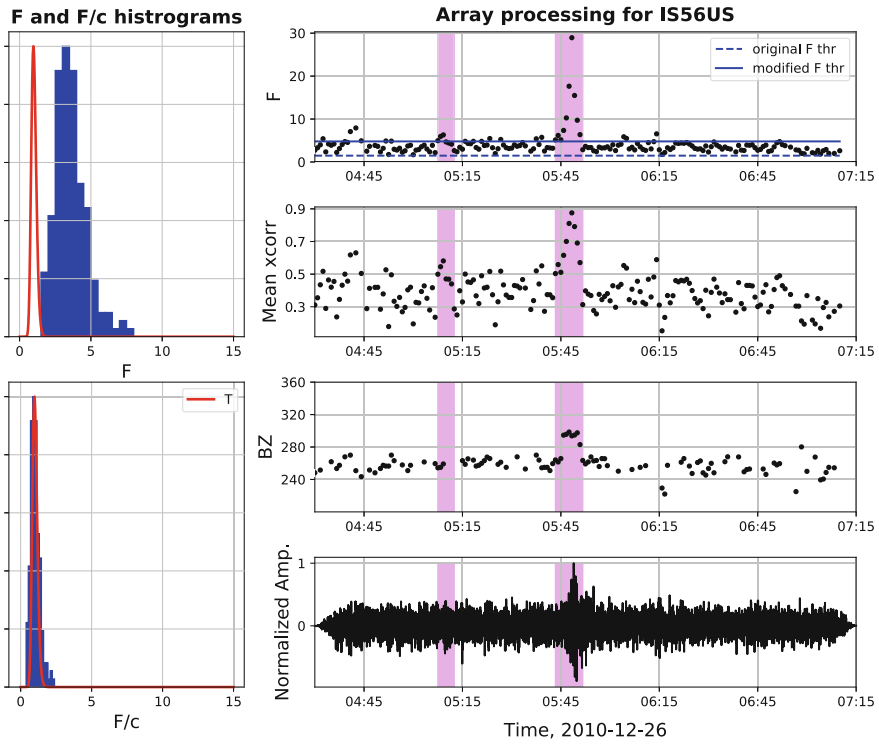

Fig. 7.4 Event detection based on Dynamic *F*-Statistics. The infrasound is from a bolide detected on December 26th, 2010 by IMS station I56US. On the left, the distribution of the theoretical F-statistics (red) and a histogram of the F-values for the array in blue (original, top, and modified, bottom). On the right, array processing results, F-values, mean cross-correlation, back azimuth, and detections (red horizontal lines)

confidence under the assumption of Gaussian noise only (the dashed blue line is the threshold for detections with false alarm probability lower than 0.01). The adaptive F-detector is used here to scale the distribution and allows for adapting to the background noise (operational-type noise) so only the transient event is detected (the solid blue line is the new threshold for detections with the same false alarm probability, 0.01). This schema has been applied to regional networks and shown to be successful at detecting transient events in the presence of interfering signals (Park et al. 2014, 2016).

An even more general approach, which is currently being explored (Arrowsmith et al. 2017), is to use a Kernel Density Estimator (KDE) (Scott 2008) to estimate the distribution of a given test statistic from a set of empirical observations of that statistic over a long-time window. Because the distribution of the test statistic is based on empirical data, it includes noise and possibly also signal, and is really a distribution of the ambient background of that test statistic. We test for $H_0 =$ ambient background signal, plus noise by taking some transform of the observed

data in a moving time window of duration T_S, which we shall denote as $S(\underline{x})$. The function, $S(\cdot)$, can be any transform that can be applied to data, resulting in a single numerical value (e.g., the semblance, correlation, etc.). If we denote a set of realizations of a specific transform in a time interval of duration T_{kde} as $(S_1, S_2, \ldots, S_n)$, then the KDE is

$$\hat{f}_h(S) = \frac{1}{Nh} \sum_{i=1}^{N} K\left(\frac{S - S_i}{h}\right), \tag{7.13}$$

where $K(\cdot)$ is the kernel (typically a Gaussian kernel) and $h > 0$ is a smoothing operator.

Figure 7.5 illustrates the concept behind a multivariate adaptive detector. Multiple test statistics are evaluated in different transform windows, denoted as T_S^i for the window corresponding to the i'th transform. A single KDE window, T_{kde}, is used to estimate the distribution of each test statistic, $\hat{f}_h(S)$.

We convert each KDE estimate to a p-value, where the p-value is defined as follows:

$$p = \int_{S_{\text{obs}}}^{\infty} \hat{f}_h(S) dS, \tag{7.14}$$

where S_{obs} is an observed, individual value of the transform.

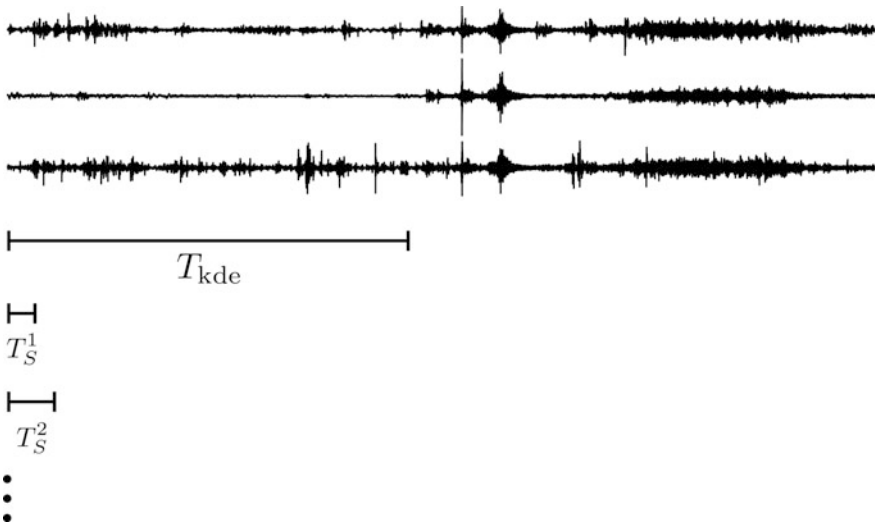

Fig. 7.5 A multivariate detector is based on the computation of multiple test statistics estimated in short time windows, with the distribution of each test statistic evaluated in a large time window of duration $\mathbf{T_{kde}}$

Given multiple transforms, which exploit different signal properties, we can combine the p-values associated with all k transforms using the Fisher's method

$$\chi^2 = -2 \sum_{i=1}^{k} \ln p_i \tag{7.15}$$

Geometrically, if different transforms are orthogonal, the use of this multivariate approach serves to increase the separation between signal and noise distributions (Fig. 7.6).

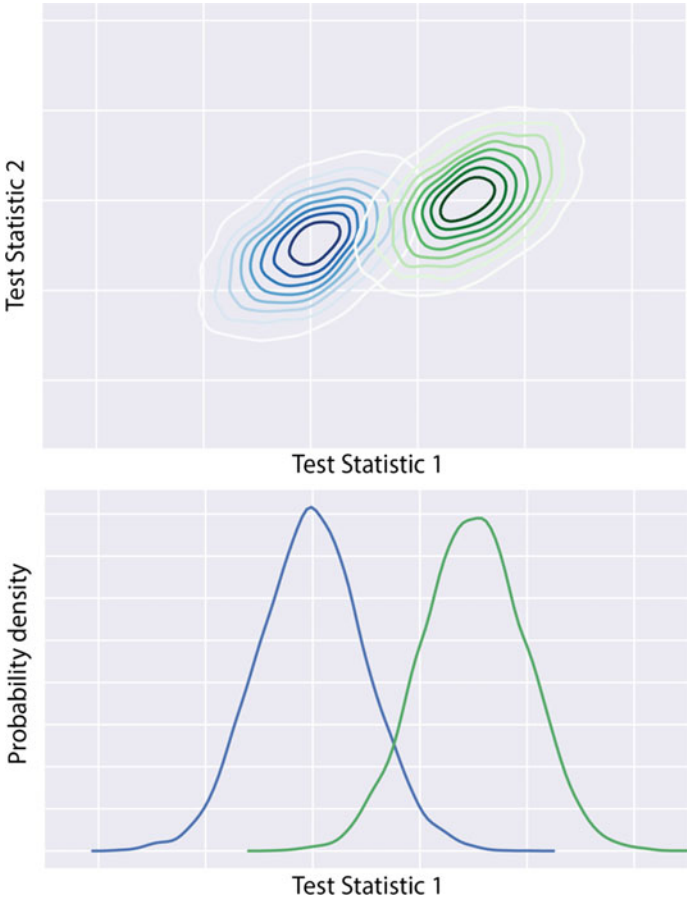

Fig. 7.6 Hypothesis testing is about defining a threshold to distinguish between signal and noise models. The threshold can be determined by considering models for both signal and noise, or by considering only the noise model. In practice, the noise model can be more easily determined from background data empirically, but having both signal and noise models is optimum. These techniques are commonly applied in one dimension (e.g., using coherence or an equivalent measure such as correlation, F-statistic, or semblance) but multivariate approach serves to increase the separation between signal and noise distributions

In our implementation, only the "ambient" distribution is defined in practice, and therefore each detection statistic is weighted by its ambient distribution in calculating a multivariate p-value. Because the ambient distribution is defined in a window of time T_{kde}, and we are not strictly required to consider the noise as physical or operational, there will always be p-values below some detection threshold and the use of at least one additional constraint is needed to prevent false alarms. Figure 7.7 illustrates the result of applying this method using two transforms, one based on the coherence of waves across a network, and a second based on the consistency of back azimuth. More details on this specific bivariate detector are provided in (Arrowsmith 2018).

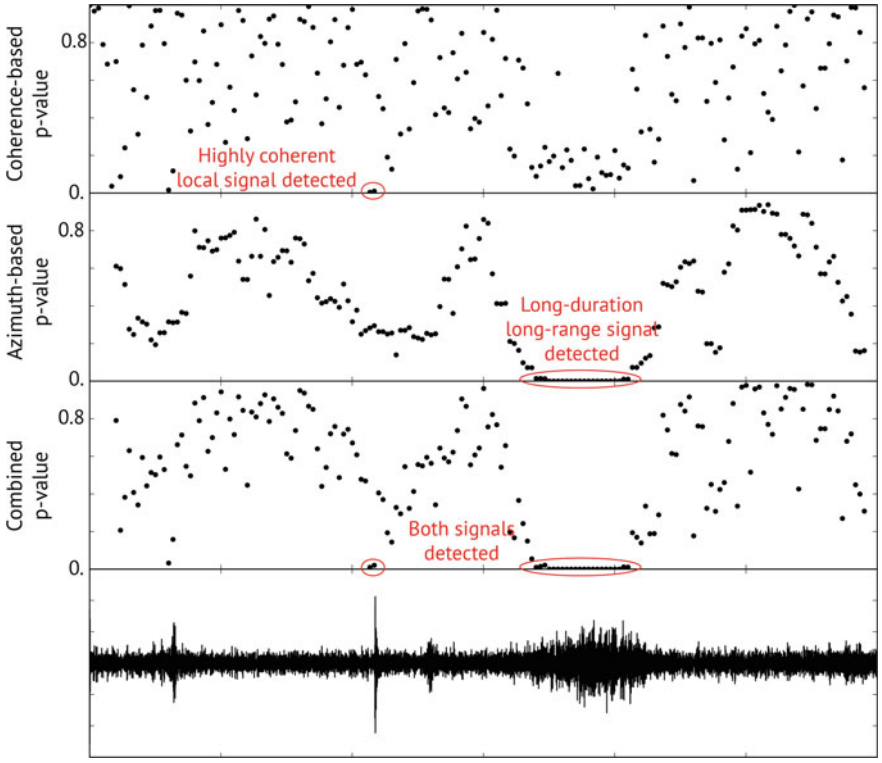

Fig. 7.7 Illustration of a multivariate detector based on coherence of waves across an array and the stability of the DOA applied to data from I56US on 02/24/2014. Each property is quantified in the form of p-values, enabling their combination via Fisher's method. While the individual detectors detect different signals, the combined approach detects both local and long-range (decorrelated) signals and provides additional information on these signal types

7.5 Parameter Estimation

After a SOI is detected the next step is to extract parameter information that can be used for characterizing the signal. In this section, we review some of most common techniques utilized for the extraction of waveform parameters. We are most interested in the extraction of the direction and speed of propagation of the SOI (estimated usually using the slowness vector) as the shape of the SOI can suffer significant changes (especially for signals propagating at global distances) and the estimation of the precise time of arrival can be difficult to estimate for very emergent signals. As we noted in the previous section, some detection test statistics can detect and extract parameter information simultaneously while others defer the parameter extraction for a second stage. For example, the F-detector will simultaneously detect and extract the slowness vector as part of its detection schema. PMCC (Cansi and Pichon 2008) calculates the TDOA to apply the consistency criteria for detection, afterwards, the already calculated TDOA are used for parameter estimation in a substage of the detection. MCCM, on the other hand, only uses the maximum cross-correlation and does not to need to compute the TDOA for its operation. Post-processing based on array geometry and estimation of the TDOA estimate the slowness vector in a subsequent processing stage. Note that for infrasound analysis, detection and parameter estimation can be performed simultaneously without much of computationally burden even for real-time applications (compare to processing for radar applications with high number of array elements and sampling rates) as the sampling rate of most system is not higher than a few 100 s of samples per second (sps), e.g., the sampling rate for the IMS stations is 20 sps, and infrasound arrays have only 4 and 15 elements. In this section, we will review the concepts behind common array processing techniques used for parameter estimation. See Olson and Szuberla (2009) for a review of the most common methods as they are applied to infrasound analysis.

The standard techniques to process array (multichannel) data can be divided into spectral-based and parametric methods (Krim and Viberg 1996). Parametric methods, such as Maximum Likelihood technique are considered to attain high-resolution but require initial information of the statistical characteristics of the data (noise and signal) and a search in a multidimensional parameter space that can be computationally complex. Spectral-based techniques such as the conventional beamforming (Bartlett), Capon (1969), or the Multiple Signal Classification, MUSIC (Schmidt 1986), require less initial information and are less complex to implement. These spectral techniques are based on constructing a spectrum-like function of a characteristic of the waveforms (e.g., beam power, coherence, and consistency), evaluating/mapping the function in the parameter space ($\boldsymbol{\theta}$), and finding the values of the parameters that maximize the spectrum.

The conventional beamforming (Bartlett) steers the covariance matrix of the observations (R) into the different elements of the 2D slowness space and looks for the values that maximize the beam power. The spectrum for the classical beamformer (Bartlett) is defined as follows:

$$\Lambda_B(\boldsymbol{\theta}) = a_{\boldsymbol{\theta}}^H R a_{\boldsymbol{\theta}}, \tag{7.16}$$

where $a_{\boldsymbol{\theta}} = a(\boldsymbol{\theta})$ is the steering vector and H is the complex conjugate operator. The Capon and MUSIC algorithms, usually called super-resolution methods, are subspace methods that rely on the decomposition of the covariance matrix R into eigenvalues (λ) and eigenvectors (v). Capon is also known as the Minimum Variance Distorsionless filter and calls for minimizing the power contributed for signals that are not in the steered direction. Capon usually shows higher performance than the classical beamformer. MUSIC can provide asymptotically unbiased estimates of the number and direction of arrival of signals, polarization, and waveforms and noise/interference strengths (Schmidt 1986). MUSIC uses a signal-noise model that is an extension of the model described by Eq. 7.2

$$x_m(t) = \sum_{j=1}^{K} s_m^j\left(t - \tau_m^j\right) + w_m(t), \tag{7.17}$$

where K is the total number of signals present in the waveform. This general signal-noise model has the advantage of potentially removing the unwanted coherent signals from operational-type noise. MUSIC relies on determining and separating eigenvalue populations for noise and signal, and thus determining the number of sources present in the observations. A spatial spectrum function is defined as follows:

$$\Lambda_{CM}(\boldsymbol{\theta}) = \left[\sum_{j=K+1}^{r} \frac{\left|a_{\boldsymbol{\theta}}^H v_j\right|^2}{\beta_j}\right]^{-1}, \tag{7.18}$$

where β_j is a coefficient, for all values of $j = 1, 2, \ldots, r$. For $K = 0$ and $\beta_j = \lambda_i$ (organized from the largest to the smallest) this expression is the Capon spectrum function (Shumway et al. 2008). If K is the number of signals and $\beta_j = 1$ this expression is the MUSIC spectrum function. MUSIC is sensitive to over-estimation of the number of sources). Other algorithms such as the Akaike Information Criteria (Akaike 1974), cumulative percentage of total variation (Jolliffe 2002) criteria, or the Bayesian Information Criterion (Wit et al. 2012) could be used for estimating the number of sources present in the data.

7.6 Evaluating Detectors

An ideal detector, i.e., the one that always identifies events without producing false detections, cannot be implemented in practice. Such an ideal detector requires an infinitely large threshold for declaration. Therefore, there is a trade-off between reducing missed event detections and reducing false ones. Too many false

detections can overwhelm the subsequent processing, i.e., association and location. However, depending on the objectives of the detection system, missing events of interest could have serious implications (e.g., the objective of the IMS is to monitor compliance for the CTBT). Thus, measuring the performance of a detector is important as that can help us tune the different parameters of the detector to reach specific requirements (Brown et al. 2000). A common methodology for assessing the performance of event detectors is the use of Receiver Operating Characteristics (ROC) curves (Arrowsmith et al. 2009; Runco Jr et al. 2014; Park et al. 2017).

A ROC curve of a detector is defined in two related ways. The first, conventional ROC curve is defined by the probability of accepting H_1 when H_1 is true (detection rate) as a function of the probability of rejecting H_0 when H_0 is true (false alarm). For the generation of a ROC for a specific detector, two large databases with available ground truth information are required. The first database consists of N_0 examples under H_0 and the other of N_1 examples under H_1. Let us consider a detection algorithm with a function test Λ. Working with the two databases we obtain two sequences of values. Figure 7.8 shows typical histograms of the two sequences. The more distant the two histograms, the easier it is to discriminate between two hypotheses. To further explore this, we compute the ROC curve as it follows: we compute the area of H_0 to the right of a given threshold value η, that gives the false alarm rate α_0. The area to the right to η of H1 gives the detection rate β_0. We report the point of coordinates (α_0, β_0) as a function of η to provide the ROC

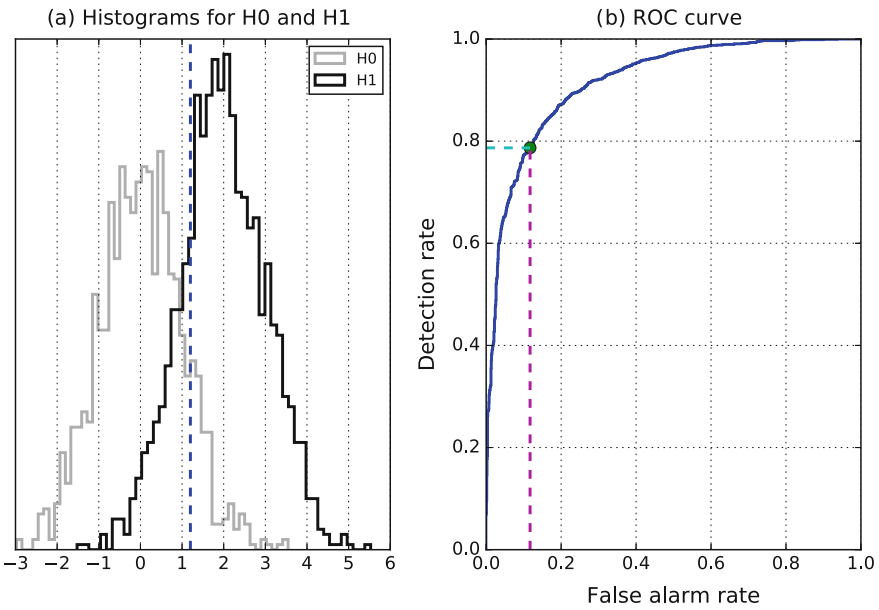

Fig. 7.8 Histograms for H_0 and H_1 and corresponding ROC curve

curve. A typical ROC curve shape is reported on panel b. The closer the curve is to the point of coordinates (0, 1), the more efficient the detector is.

The datasets required to construct a ROC can have multiple forms and it is important that the characteristics of the H_0 and H_1 resemble the type of noise and signals that the detector will operate on. A common approach for the construction of datasets for detector testing is the implantation of events (real or synthetic SOI-type waveforms) in real or synthetic background noise (Brown et al. 2000; Kohl et al. 2005; Charbit and Mialle 2015). The amplitudes of the embedded signals can be scaled to mimic the arrival of signals under different signals-to-noise ratios. To detect such scaled, embedded signals, it is practical to construct the second type of ROC curve that compares detection rates against some measure of the embedded signal SNR (Richards 2005). More explicitly, these ROC curves are defined by the probability of accepting H_1 when H_1 is true (detection rate) as a function of signal/waveform SNR, for a fixed probability of rejecting H_0 when H_0 is true (false alarm). The predictive capability of a detector is then evaluated by comparing these semi-empirical ROC curves against semi-theoretical ROC curves. The semi-empirical ROC curves are constructed in four stages by (1) scaling the amplitude of a reference infrasound waveform that records a known source, (2) embedding these data into records of real noise, (3) processing these data with a digital detector, and (4) counting true detections. In this case, the signal's original amplitude is scaled to a prescribed value selected from a scaled, "relative" SNR grid ΔSNR defined as

$$\Delta SNR = 20\log_{10}\left(\frac{A_S}{A_N}\right) - 20\log_{10}\left(\frac{A_{S,0}}{A_{N,0}}\right) \tag{7.19}$$

Equation 7.19 compares the root-mean-square amplitude A_S of the scaled waveform to root-mean-square amplitude A_N of the background noise, relative to the signal amplitude $A_{S,0}$ and noise amplitude $A_{N,0}$ of the original data. Scalar ΔSNR has units of decibels. The scaled waveform is then superimposed with recorded noise sampled from a selected time period and processed with the detector. Each processing window includes a detection threshold η that is consistent with a constant false alarm rate α_0, as computed from the F-distribution that is best parameterized for the data (see Eq. 7.8). Data statistics that exceed η, at the prescribed waveform embedding time, are counted as true detections. Similarly, missed detections are counted where the detector fails to register an event at a known waveform infusion time. This process is repeated over many noise records for each SNR value. Therefore, the detector processes waveforms over a grid of ΔSNR values, for each noise field record. Naturally, these records of the noise field also include significant signal clutter. Therefore, the scaled, embedded waveforms occasionally superimposed with other infrasound signals that not attributable to a known source (in contrast to H_0). This signal interference creates variability in the observed detector performance. Such events elevate false detection counts whenever waveforms localize outside the detector window.

Theoretical ROC curves are generated in parallel with the semi-empirical detection process. In this case, the statistical parameters of the *F*-distributed detection statistic (Eq. 7.10) that were estimated from the data are used to construct PDFs under the signal-present hypothesis. This PDF is further parameterized by a noncentrality parameter that depends on the effective degrees of freedom within the data and the signal amplitude, which is prescribed by the ΔSNR grid value. This parameter estimates that shape these *F*-distributions are updated in each processing window, as the noise is likely to be nonstationary over sufficiently long-time durations. The theoretical waveform detection probability β_0 is then the right-tail integral of these PDFs, taken from the concurrent threshold η to infinity. Last, this probability is scaled by the number of waveform counts to compare against semi-empirical counts.

Figure 7.9 compares empirical ROC curves against predicted ROC curves using this method. The infrasound source, in this case, is a 1.7 kg solid charge detonated at 1 m above the ground. The separated gray stair plots illustrate five days of detection counts using infused and scaled waveforms. The solid black curves show five days of predicted cumulative probability counts. In each case, predictions are made from PDFs that employ shaping parameters like $\hat{c}$, that were estimated directly from the data and updated hourly (see the discussion following Sect. 7.4.3

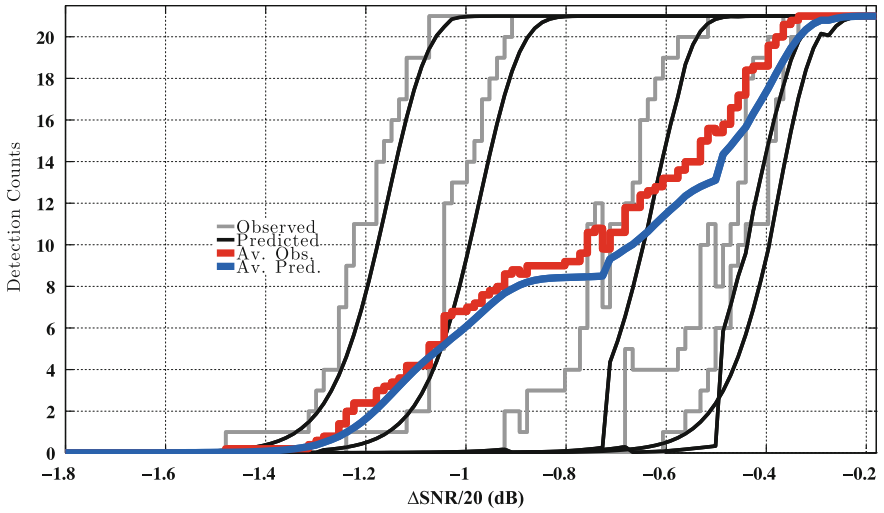

Fig. 7.9 Semi-empirical ROC curves computed over five distinct days of noise records (stair plots) shown with associated, theoretical ROC curves (smooth curves). Data include 4–20 Hz acoustic waveforms beamformed on a small aperture, four element array that records a 1.7 kg Composition-B solid charge detonated 1 m over dry ground. Detection counts are computed from an *F*-detector operating at a 10^{-3} constant false alarm rate and plotted against scaled ΔSNR (Eq. 7.19) to improve readability. Thickest curves show empirical (red stair plot) and theoretical (blue plot) averages over the five-day collection period. Each processing window includes 21 infused waveforms

for parametric definitions). The blue solid curves show the average of these predicted ROC curves; the red stair plot shows the average empirical ROC curves. The time-averaged predictions agree well with the observed detections. The slight outperformance by the observed ROC likely results from the multiple detection opportunities afforded the detector over each waveform segment that is not quantified by the predicted, noncentral *F*-distribution. Despite such slight performance discrepancies, such ROC curve comparisons do provide a quantitative comparison between the predicted versus observed performance of infrasound detectors in real noise environments. This second type of ROC curve is additionally useful for estimating threshold SNR values at which a detector provides a desired probability of detecting an infrasound waveform. In summary, there is a clear need for future research in this area to explore the performance of detectors under both physical- and operational-type noise and the construction of infrasound specific datasets that can be used for assessing the performance of different detection methodologies.

7.7 Conclusions

The detection of infrasonic signals generated by atmospheric explosions is very challenging given the wide range of characteristics of the signals and complexity of the acoustic wavefield (acoustic backgrounds). We have defined physical- and operational-type noise and show how this separation can improve signal and noise models, as well as detector evaluation efforts. We show that the classical mathematical description of signals and noise for detection is based only on physical-type noise and its characteristics, mainly de-correlation, but in practice, we have to use operational-type noise instead. We discussed strategies to compensate for the use of operational-type noise when the physical-type noise is assumed and described a methodology to combine different detectors based on different aspects of the waveform to improve detection. Combining different estimates of the waveform can significantly help in the detection process and more research in this direction may be required especially as we hope to reduce thresholds in order to detect smaller events. Last, direct comparison between semi-empirical and semi-theoretical Receiver Operating Characteristic (ROC) curves provide a quantitative method to assess the predictive capability of infrasound detectors.

References

Akaike H (1974) A new look at the statistical model identification. IEEE Trans Autom Control 19 (6):716–723

Anderson JF, Johnson JB, Arechiga RO, Thomas RJ (2014) Mapping thunder sources by inverting acoustic and electromagnetic observations. J Geophys Res: Atmos 119(23):13,287–213,304

Arrowsmith S (2018) False alarms and the IMS infrasound network: Towards a quantitative understanding of the factors influencing the creation of false events. Geophys J Int (Submitted)

Arrowsmith S, Euler G, Marcillo O, Blom P, Whitaker R, Randall G (2015) Development of a robust and automated infrasound event catalogue using the International Monitoring System. Geophys J Int 200(3):1411–1422

Arrowsmith S, Nippress A, Green D (2017) False alarms and the IMS infrasound network: towards a quantitative understanding of the factors influencing the creation of false events. Geophys J Int (In Prep)

Arrowsmith SJ, Taylor SR (2013) Multivariate acoustic detection of small explosions using Fisher's combined probability test. J Acoust Soc Am 133(3):El168–El173

Arrowsmith SJ, Whitaker R, Katz C, Hayward C (2009) The F-detector revisited: an improved strategy for signal detection at seismic and infrasound arrays. Bull Seismol Soc Am 99(1):449–453

Blandford RR (1974) Automatic event detector at Tonto-Forest seismic observatory. Geophysics 39(5):633–643

Bowman JR, Baker GE, Bahavar M (2005) Ambient infrasound noise. Geophys Res Lett 32(9):1–5

Brachet N, Brown D, Le Bras R, Cansi Y, Mialle P, Coyne J (2010) Monitoring the earth's atmosphere with the global IMS infrasound network. In: Infrasound monitoring for atmospheric studies, Springer, pp 77–118

Brown DJ, Katz CN, Wang J, Whitaker RW (2000) Tuning of automatic signal detection algorithms for IMS style infrasound arrays. In: 22nd Annual DoD/DoE seismic research symposium, New Orleans, LA, DTIC Document

Brown DJ, Whitaker R, Kennett BLN, Tarlowski C (2008) Automatic infrasonic signal detection using the Hough transform. J Geophys Res: Atmos 113(D17):D17105

Cansi Y (1995) An automatic seismic event processing for detection and location: the P.M.C.C. Method. Geophys Res Lett 22(9):1021–1024

Cansi Y, Pichon AL (2008) Infrasound event detection using the progressive multi-channel correlation algorithm. In: Havelock D, Kuwano S, Vorländer, M (eds) Handbook of signal processing in acoustics. Springer, New York, NY, pp 1425–1435

Capon J (1969) High-resolution frequency-wavenumber spectrum analysis. Proc IEEE 57 (8):1408–1418

Ceranna L, Le Pichon A, Green DN, Mialle P (2009) The Buncefield explosion: a benchmark for infrasound analysis across Central Europe. Geophys J Int 177(2):491–508

Ceranna L, Matoza R, Hupe P, Le Pichon A, Landès M (2019) Systematic array processing of a decade of global IMS infrasound data. In: Le Pichon A, Blanc E, Hauchecorne A (eds) Infrasound monitoring for atmospheric studies, 2nd edn. Springer, Dordrecht, pp 471–482

Charbit M (2017) Digital Signal Processing (DSP) with python programming. Wiley

Charbit MJ, Mialle P (2015) Application of the framework for detection software evaluation. In: CTBT: science and technology 2015 conference. Vienna, Austria, T3.3-P5

Christie DR, Campus P (2009) The IMS infrasound network: design and establishment of infrasound stations. In: Le Pichon A, Blanc E, Hauchecorne A (eds) Infrasound monitoring for atmospheric studies. Springer Netherlands, Dordrecht, pp 29–75

Dabrowa AL, Green DN, Rust AC, Phillips JC (2011) A global study of volcanic infrasound characteristics and the potential for long-range monitoring. Earth Planet Sci Lett 310(3–4):369–379

Dahlman O, Israelson H, Wagner H (1971) Ground motion and atmospheric pressure waves from nuclear explosions. Nat-Phys Sci 232(30):79–+

Don WL, Ewing M (1962) Atmospheric waves from nuclear explosions. J Geophys Res 67(5):1855–&

Donn WL, Ewing M (1962) Atmospheric waves from nuclear explosions. 2. The soviet test of 30 October 1961. J Atmos Sci 19(3):264–273

Donn WL, Naini B (1973) Sea wave origin of microbaroms and microseisms. J Geophys Res 78 (21):4482–4488

Drob DP, Picone JM, Garcés M (2003) Global morphology of infrasound propagation. J Geophys Res 108(D21):1–12

Fee D, Matoza RS (2013) An overview of volcano infrasound: from Hawaiian to Plinian, local to global. J Volcanol Geoth Res 249:123–139

Fee D, Waxler R, Assink J, Gitterman Y, Given J, Coyne J, Mialle P, Garces M, Drob D, Kleinert D, Hofstetter R, Grenard P (2013) Overview of the 2009 and 2011 Sayarim infrasound calibration experiments. J Geophys Res-Atmos 118(12):6122–6143

Fehr U (1967) Measurements of infrasound from artificial and natural sources. J Geophys Res 72(9):2403–2417

Green DN (2015) The spatial coherence structure of infrasonic waves: analysis of data from international monitoring system arrays. Geophys J Int 201(1):377–389

Green DN, Vergoz J, Gibson R, Le Pichon A, Ceranna L (2011) Infrasound radiated by the Gerdec and Chelopechene explosions: propagation along unexpected paths. Geophys J Int 185(2):890–910

Jolliffe IT (2002) Principal component analysis. Springer, New York

Kay SM (2013) Fundamentals of statistical signal processing: practical algorithm development. Pearson Education

Kohl B, Bennett TJ, Bondár I, Barker B, Nagy W, Reasoner C (2005) Development of a network data set for evaluating detection and network processing performance. In: 27th seismic research review: ground-based nuclear explosion monitoring technologies, Rancho Mirage, CA

Krim H, Viberg M (1996) Two decades of array signal processing research—the parametric approach. IEEE Signal Process Mag 13(4):67–94

Landès M, Ceranna L, Le Pichon A, Matoza RS (2012) Localization of microbarom sources using the IMS infrasound network. J Geophys Res 117(D6):D06102

Le Pichon A, Ceranna L, Pilger C, Mialle P, Brown D, Herry P, Brachet N (2013) The 2013 Russian fireball largest ever detected by CTBTO infrasound sensors. Geophys Res Lett 40(14):3732–3737

Lee DC, Olson JV, Szuberla CAL (2013) Computationally robust and noise resistant numerical detector for the detection of atmospheric infrasound. J Acoust Soc Am 134(1):862–868

Mack H, Flinn EA (1971) Analysis of the spatial coherence of short-period acoustic-gravity waves in the atmosphere. Geophys J Int 26(1–4):255–269

Marcillo O, Arrowsmith S, Blom P, Jones K (2015) On infrasound generated by wind farms and its propagation in low-altitude tropospheric waveguides. J Geophys Res: Atmos 120(19):9855–9868

Marty J (2019) The IMS infrasound network: current status and technological developments. In: Le Pichon A, Blanc E, Hauchecorne A (eds) Infrasound monitoring for atmospheric studies, 2nd edn. Springer, Dordrecht, pp 3–62

Matoza R, Fee D, Green D, Mialle P (2019) Volcano infrasound and the international monitoring system. In: Le Pichon A, Blanc E, Hauchecorne A (eds) Infrasound monitoring for atmospheric studies, 2nd edn. Springer, Dordrecht, pp 1023–1077

Mialle P, Brown D, Arora N, colleagues from IDC (2019) Advances in operational processing at the international data centre. In: Le Pichon A, Blanc E, Hauchecorne A (eds) Infrasound monitoring for atmospheric studies, 2nd edn. Springer, Dordrecht, pp 209–248

Morgan S, Raspet R (1992) Investigation of the mechanisms of low-frequency wind noise generation outdoors. J Acoust Soc Am 92(2):1180–1183

Neidell NS, Taner MT, Koehler F (1969) Semblance and other coherency measures for multichannel data. Geophysics 34(6):1012–&

Nouvellet A, Charbit M, Le Pichon A, Roueff F, Che IY (2013) Coherence parameters estimation from noisy observations. In: Infrasound technology workshop, Vienna

Olson JV, Szuberla CAL (2009) Processing infrasonic array data. In: Handbook of signal processing in acoustics, pp 1487–1496

Park J, Arrowsmith SJ, Hayward C, Stump BW, Blom P (2014) Automatic infrasound detection and location of sources in the western United States. J Geophys Res: Atmos 119(13):7773–7798

Park J, Hayward CT, Zeiler CP, Arrowsmith SJ, Stump BW (2017) Assessment of infrasound detectors based on analyst review, environmental effects, and detection characteristics. Bull Seismol Soc Am 107(2):674–690

Park J, Stump BW, Hayward C, Arrowsmith SJ, Che IY, Drob DP (2016) Detection of regional infrasound signals using array data: testing, tuning, and physical interpretation. J Acoust Soc Am 140(1):239–259

Pilger C, Ceranna L (2017) The influence of periodic wind turbine noise on infrasound array measurements. J Sound Vib 388:188–200

Richards MA (2005) Fundamentals of radar signal processing. McGraw-Hill

Runco AM Jr, Louthain JA, Clauter DA (2014) Optimizing the PMCC algorithm for infrasound and seismic nuclear treaty monitoring. Open J Acoust 4(04):204

Schmidt RO (1986) Multiple emitter location and signal parameter-estimation. IEEE Trans Antennas Propag 34(3):276–280

Scott, DW (2008) Kernel density estimators. In: Multivariate density estimation. Wiley, pp 125–193

Silber E, Brown P (2019) Infrasound monitoring as a tool to characterize impacting near-earth objects (NEOs). In: Le Pichon A, Blanc E, Hauchecorne A (eds) Infrasound monitoring for atmospheric studies, 2nd edn. Springer, Dordrecht, pp 939–986

Shumway RH, Kim S-E, Blandfor R (1999) Nonlinear estimation for time series observed on arrays. In: Ghosh S (ed) Asymptotics, nonparametrics, and time series. CRC Press, p 227

Shumway RH, Smart E, Clauter DA (2008) Mixed signal processing for regional and teleseismic arrays. Bull Seismol Soc Am 98(1):36–51

Stopa JE, Cheung KF, GarcÈs MA, Fee D (2011) Source of microbaroms from tropical cyclone waves. Geophys Res Lett 38(5):L05602

Taylor SR, Arrowsmith SJ, Anderson DN (2013) Development of a matched filter detector for acoustic signals at local distances from small explosions. J Acoust Soc Am 134(1):El84–El90

Walker KT (2012) Evaluating the opposing wave interaction hypothesis for the generation of microbaroms in the eastern North Pacific. J Geophys Res-Ocean 117

Wit E, van den Heuvel E, Romeijn JW (2012) All models are wrong…': an introduction to model uncertainty. Stat Neerl 66(3):217–236